

## FRACTURE MECHANICS ANALYSIS OF STITCHED STIFFENER-SKIN DEBONDING

E.H. Glaessgen,\* I.S. Raju† and C.C. Poe, Jr.‡  
NASA Langley Research Center, Hampton, VA 23681-0001, U.S.A.

### Abstract

An analysis based on plate finite elements and the virtual crack closure technique has been implemented to study the effect of stitching on mode I and mode II strain energy release rates for debond configurations. The stitches were modeled as discrete nonlinear fastener elements with a compliance determined by experiment. The axial and shear behavior of the stitches was considered, however, the two compliances and failure loads were assumed to be independent. Both a double cantilever beam (mode I) and a mixed mode skin-stiffener debond configuration were studied. In the double cantilever beam configurations,  $G_I$  began to decrease once the debond had grown beyond the first row of stitches and was reduced to zero for long debonds. In the mixed-mode skin-stiffener configurations,  $G_I$  showed a similar behavior as in the double cantilever beam configurations, however,  $G_{II}$  continued to increase with increasing debond length.

### Introduction

Stitched warp-knit textile composite materials are currently being considered for use in primary aircraft structures.<sup>1</sup> In the NASA Advanced Subsonic Technology (AST) program, a stitched composite wing skin is being developed to demonstrate both the manufacturing and analytical technology needed to produce such structures. Structural panels, such as the one shown in Figure 1, are made of stiffening elements that are mechanically attached to the skin with stitches in the dry preform state before the resin is introduced via resin film infusion (RFI).<sup>1</sup>

The panel configuration shown in Figure 1 contains several important features: the skin, stiffeners, and intercostals. These panels are typically made of between two and ten stacks of 0.055 in. thick carbon warp-knit

fabric that are layered and stitched with Kevlar yarns to form a skin. The stiffeners and intercostals are made of a similar number of stacks of stitched fabric and are stitched to the skin. Once the preform is assembled, the entire structure is infused with epoxy resin.

Stiffened panels are typically subjected to large in-plane and out-of-plane loads that produce considerable bending and shearing stresses at skin-stiffener interfaces.<sup>2</sup> Much of the research on skin-stiffener debonding has focused on the calculation of these skin-stiffener interface stresses.<sup>3-5</sup> The stresses may be large enough to cause a separation between the skin and stiffening elements resulting in a delamination or debond. Fracture mechanics-based approaches have been widely used to characterize delaminations and debonds in unstitched structures. Two-dimensional plane strain models have been used for analysis of skin-stiffener debonding.<sup>6-8</sup> Models based on quasi-3D or 3D brick finite element models have been used to study edge delamination and near-surface delamination of composites.<sup>9-11</sup> Since many layers of brick elements are often required to model both the skin panel and the associated stiffeners, finite element models with large numbers of degrees-of-freedom may be required.

In an effort to develop computationally efficient models, references 12-15 proposed the use of plate elements to model skin-stiffener debond problems and calculate strain energy release rate using the virtual crack closure technique (VCCT). Conventional plate modeling inherently assumes that the reference surface of the plate coincides with the middle surface. Thus, the skin and stiffener are usually modeled by plate elements with nodes at their respective mid-planes. This conventional method is not convenient for modeling debonding because it entails complex constraints to tie the flange nodes to the corresponding skin nodes. Thus, the approach taken in references 12-16 and the present analysis, is to place the skin nodes and the stiffener nodes along the interface between the skin and the stiffener. The positioning of these nodes at the interface is performed by defining an offset distance from the mid-plane of both the skin and the stiffener. Plate-element models using this technique can be used to evaluate accurate values of mode I and mode II strain energy release rates.<sup>16</sup>

Suppression of the growth of debonds between the stiffeners and skin may be achieved by stitching the

\* Research Associate, National Research Council

† Head, Mechanics of Materials Branch, Associate Fellow AIAA

‡ Senior Scientist, Mechanics of Materials Branch

Copyright 1998 by the American Institute of Aeronautics and Astronautics, Inc. No copyright is asserted in the United States under Title 17, U.S. Code. The U.S. Government has a royalty-free license to exercise all rights under the copyright claimed herein for Governmental Purposes. All other rights are reserved by the copyright owner.

stiffeners to the skin. The effects of stitching on delamination or debond growth in composites have been examined in simple configurations with some success.<sup>17-23</sup> In these works, the stitches are modeled as truss or beam elements connecting nodes through the thickness of the material. References 17-21 modeled laminates as two-dimensional plane strain structural components, while references 22-23 modeled the laminates as three-dimensional solids. An advantage of the three-dimensional modeling is to allow the stitches to be modeled discretely rather than as structural components with an "effective" stiffness.

The objective of this paper is to quantify the effect of stitches on the mode I and mode II strain energy release rates of double cantilever beam and mixed mode skin-stiffener debond configurations. The plate element modeling technique is used to analyze the debond configurations and the VCCT is used to calculate strain energy release rates. Because the nodes of the plate elements are offset to the interface between the skin and stiffener, the plate element models do not allow for nodal connectivity beyond the element interface along the debonds. The stitches are not modeled as finite length spar or beam elements as in references 17-23, but rather as nonlinear fastener elements with axial and shear compliances determined by experiment. In this paper, the effect of parameters such as stitch stiffness, applied load and debond length on the strain energy release rates are studied.

### Analysis

In this section, the analyses for the double cantilever beam and debond configurations are presented. Next, the method used for computing strain energy release rates using the VCCT is briefly discussed. Lastly, strategies for modeling the stitches are presented.

#### Double Cantilever Beam and Mixed-Mode Debond Configurations

Figure 1 shows the configuration and loading of a typical skin-stiffened stitched composite panel. Three-dimensional modeling and analysis of this complex configuration would require a large finite element model with many thousands of degrees of freedom. However, considerable insight into the behavior of the complicated configurations can be gained by examining simpler configurations such as those shown in Figure 2 while reducing modeling complexity. Figure 2 shows the two simple configurations, the double cantilever beam (DCB) and the mixed-mode skin-stiffener debond configuration. Both of the configurations were modeled as infinitely wide strips with cylindrical bending repeating unit boundary conditions ( $v=0$ ,  $\theta_x=0$  on  $y=\pm S_y/2$  in Figure 2).

For both the DCB and mixed-mode debond configurations, a stitch pattern of 8 rows/in. by 8 stitches/in. was assumed. That is, the stitch spacings,  $s_x$  and  $s_y$ , are 0.125 inches in the  $x$ - and  $y$ - directions, respectively (see Figure 2). Axial and shear stitch stiffnesses and forces are denoted by  $K_{axial}$ ,  $K_{shear}$  and  $F_{axial}$  and  $F_{shear}$ , respectively, in Figure 2. Material and skin thicknesses that are representative of the stitched composite wing skin used in the NASA Advanced Subsonic Technology (AST) program are considered.<sup>1</sup>

A representation of the finite element mesh used in these analyses is shown for both the DCB and mixed-mode debond configurations in Figures 2(a) and 2(b), respectively. The element size chosen was 0.005 in. in the  $x$ -direction by 0.03125 in. in the  $y$ -direction for both models.

The material is a carbon/epoxy system representative of materials used in the AST stitched composite wing skin.<sup>1</sup> In both the DCB and mixed-mode debond analyses, the same material is assumed for both the skin and the stiffener flange. Each stack of material is oriented with its primary axis in the  $x$ -direction and is composed of forty-four percent zero degree fibers, forty-four percent forty-five degree fibers and twelve percent ninety degree fibers. The equivalent laminate stacking sequence is  $(45/-45/0/90/0/-45/45)_s$  with areal weights of 0.577 oz./ft.<sup>2</sup>, 1.21 oz./ft.<sup>2</sup> and 0.651 oz./ft.<sup>2</sup> for the forty-five, zero and ninety degree plies, respectively. In these analyses, the laminates are assumed to be homogeneous with properties

$$\begin{aligned} E_{11} &= 9.25 \times 10^6 \text{ psi} & E_{33} &= E_{22} = 4.67 \times 10^6 \text{ psi} \\ \mu_{12} &= \mu_{13} = 2.27 \times 10^6 \text{ psi} & \mu_{23} &= 0.497 \times 10^6 \text{ psi} \\ \nu_{12} &= \nu_{13} = 0.397 & \nu_{23} &= 0.490 \end{aligned}$$

where  $E_{ij}$ ,  $\mu_{ij}$ ,  $\nu_{ij}$  ( $i,j=1,2,3$ ) are the Young's moduli, shear moduli, and Poisson's ratio, respectively, and the subscripts 1,2,3 represent the fiber and two transverse directions, respectively.

#### Strain Energy Release Rates

The virtual crack closure technique (VCCT)<sup>24-25</sup> can be used to calculate strain energy release rates,  $G$ , with plate elements using the techniques discussed in references 14-16. The STAGS 480, 9-node quadratic shear deformable, plate/shell element<sup>26-27</sup> is used for modeling the debond configurations. A representation of the 9-noded plate elements near a debond front is shown in Figure 3. Reference 16 suggests that allowing the elements ahead of the debond front to have free rotations ensures accurate evaluation of the strain energy release rates. If there are free rotations ahead of the debond front, then the  $G$  values can be calculated using the nodal forces ( $F_x$ ,  $F_y$ ,  $F_z$ ) and displacements ( $u$ ,  $v$ ,  $w$ )

near the debond front and the increment of new debond area created as (see Figure 3)<sup>12</sup>

*Mode-I components:*

$$\begin{aligned}(G_I)_i &= -\frac{1}{2\Delta b_i} [F_{z_i}(w_p - w_{p'}) + F_{z_i}(w_l - w_{l'})] \\ (G_I)_j &= -\frac{1}{2\Delta b_j} [F_{z_j}(w_q - w_{q'}) + F_{z_j}(w_m - w_{m'})] \quad (1) \\ (G_I)_k &= -\frac{1}{2\Delta b_k} [F_{z_k}(w_r - w_{r'}) + F_{z_k}(w_n - w_{n'})]\end{aligned}$$

*Mode-II components:*

$$\begin{aligned}(G_{II})_i &= -\frac{1}{2\Delta b_i} [F_{x_i}(u_p - u_{p'}) + F_{x_i}(u_l - u_{l'})] \\ (G_{II})_j &= -\frac{1}{2\Delta b_j} [F_{x_j}(u_q - u_{q'}) + F_{x_j}(u_m - u_{m'})] \quad (2) \\ (G_{II})_k &= -\frac{1}{2\Delta b_k} [F_{x_k}(u_r - u_{r'}) + F_{x_k}(u_n - u_{n'})]\end{aligned}$$

*Mode-III components:*

$$\begin{aligned}(G_{III})_i &= -\frac{1}{2\Delta b_i} [F_{y_i}(v_p - v_{p'}) + F_{y_i}(v_l - v_{l'})] \\ (G_{III})_j &= -\frac{1}{2\Delta b_j} [F_{y_j}(v_q - v_{q'}) + F_{y_j}(v_m - v_{m'})] \quad (3) \\ (G_{III})_k &= -\frac{1}{2\Delta b_k} [F_{y_k}(v_r - v_{r'}) + F_{y_k}(v_n - v_{n'})]\end{aligned}$$

with

$$(G_{Total})_\gamma = (G_I + G_{II} + G_{III})|_\gamma, \text{ and} \quad (4)$$

$\gamma = i, j \text{ and } k.$

The elements are assumed to have the same length,  $\Delta$ , ahead of and behind the debond front. The equivalent widths apportioned to the two corner debond-front nodes are  $b_i$  and  $b_k$ , and to the midside debond front node is  $b_j$ . These are given by equation (5) as

$$\begin{aligned}b_i &= \frac{1}{6}[b_{J-1} + b_J], \\ b_j &= \frac{2}{3}b_J, \\ b_k &= \frac{1}{6}[b_J + b_{J+1}],\end{aligned} \quad (5)$$

where  $b_{J-1}$ ,  $b_J$  and  $b_{J+1}$  are the widths of layers  $J-1$ ,  $J$  and  $J+1$ , respectively, as shown in Figure 3(b). Note that

this modeling strategy, that assumes no rotational constraints ahead of the debond front, is termed "Technique-B" in references 14-15.

Both the models of the double cantilever beam and the mixed-mode skin-stiffener debond configuration assume self-similar debond growth between the skin and stiffener. Thus, no variation in  $G$  across the width of the model is assumed and the values of  $G$  reported are those calculated along the lines of the stitching ( $y=0$  in Figure 2). Although a tendency for the debond to leave the skin-stiffener interface has been shown in some composite skin-stiffener structures,<sup>6-8</sup> experimental evidence suggests that the self-similar assumptions are valid for this type of stitched woven composite.<sup>28</sup>

The strain energy release rates along the debond front of the DCB and mixed-mode skin-stiffener debond configurations are calculated using equations (1)-(5). The nonlinear nature of the compliance curves necessitates a geometrically nonlinear finite element analysis. Both of the configurations have been analyzed using the STAGS finite element code.

### Stitch Modeling

Unlike the two-dimensional and three-dimensional models considered in references 17-21, the plate element-based modeling technique does not allow through-the-thickness modeling of details such as the stitches; nor does it allow nodal connections other than at the plate element reference surface. Thus, in the present technique, the stitches are not modeled as spar or beam elements, but rather as "fastener elements." The fastener elements are imposed as nonlinear constraints within the plate element model.<sup>26-27</sup> These "fastener elements" have both an axial and a shear stiffness,  $K_{axial}$  and  $K_{shear}$ , respectively, and are schematically shown as springs in Figure 2(a). Only the fastener elements behind the debond front ( $L < x < L+a$  in Figure 2a) carry load since the upper and lower plate elements ahead of the debond front are coupled using constraint equations to have identical translational displacements.

Accurate compliance curves for both axial and shear behavior of the stitches were developed in reference 29 using flatwise tension and double lap shear tests (see Figure 4), respectively. A piecewise linear representation of this data is used in the finite element model. The points used in the linearization of the compliance curves are shown in Figure 4. Examination of the flatwise tensile test data revealed that the axial compliance of the stitches increases from approximately  $1.30E-5$  in./lb. (77000 lb./in. stiffness) initially to  $4.88E-4$  in./lb. (2050 lb./in. stiffness) near failure. Similar examination of the double lap shear test data

showed that the shear compliance of the stitches increases from approximately  $5.50\text{E-}5$  in./lb. (18200 lb./in. stiffness) initially to  $6.25\text{E-}4$  in./lb. (1600 lb./in. stiffness) near failure. The axial and shear responses of the stitches are assumed to be independent. Also note that failure of the stitches occurred at 58 lb. in tension and 38 lb. in shear. These stiffnesses and failure loads will be used for the characterizations in this paper. For the purposes of these analyses, the axial and shear responses of the stitches are assumed to be independent.

## Results and Discussion

### Double Cantilever Beam (DCB) Models

#### Effect of Stitch Stiffness

A mode I loading of 125 lb./in. was applied to the configuration shown in Figure 5(a) with a debond length,  $a$ , of 0.250 in. The axial stiffness of the stitches was increased in decades from 1.0 lb./in. to 100,000 lb./in. to evaluate its effect on the DCB configuration with several sublaminate thicknesses,  $t$ , of 0.110, 0.220 and 0.440 inches. Figure 5 presents the strain energy release rate,  $G$ , and the axial stitch force,  $F_{axial}/F_{failure}$ , for the DCB configuration. A stitch stiffness in excess of 1,000 lb./in. is required to noticeably effect the value of  $G_I$  for even the most compliant ( $t=0.110$  in.) DCB. As shown in Figure 5(a), for a given applied load,  $P$ , the effect of the stitching on  $G_I$  appears to decrease with increasing DCB thickness for the range of stitch stiffnesses considered. At stitch stiffnesses approaching 100,000 lb./in. the strain energy release rate of the thinnest (most compliant) DCB approaches that of the stiffest DCB since the stitches have more effect in the compliant DCB configurations than in the stiffer configurations. As a result, the load carried by the stitches increases with increasing DCB compliance as shown in Figure 5(b). Comparison of the measured initial axial stitch stiffness of about 80,000 lb./in., from the flatwise tensile test data, with the curves of Figure 5(a) reveals that this initial stitch stiffness will have a significant effect on strain energy release rate.

#### Effect of Increasing Load

Finite element models utilizing the compliance curves shown in Figure 4(a) were used to evaluate the response of the DCB to increasing load. As shown in Figure 6(a),  $G_I$  increases dramatically with increasing applied load for all three DCB configurations. As expected, the thinnest ( $t=0.110$  in.) DCB shows the largest sensitivity to the increase in load. Figure 6(b) shows

the increase in load,  $F_{axial}/F_{failure}$ , in the stitches with increasing applied load for the three DCB configurations. However, Figure 4(a) shows that as the load in the stitch increases, the corresponding stitch stiffness decreases. Also note that the maximum values of strain energy release rate shown in Figure 6(a) are well beyond the value required to propagate the debond in an epoxy resin;  $G_{IC}$  for a brittle epoxy resin is approximately 1.0 in.-lb./in.<sup>230</sup>

The effect of the nonlinearity of the stitches is most evident when the load in the stitches is allowed to increase to the large values shown in Figure 6(b). For example, in the thinnest ( $t=0.110$  in.) case with an applied load of 1,000 lb./in., the load of approximately 42 lb. ( $F_{axial}/F_{failure}=0.73$  in Figure 6b) in the stitches corresponds to a stitch stiffness of 2,600 lb./in. This represents a decrease of stitch stiffness by a factor of 30 compared with the initial value. Thus, the effectiveness of each stitch is expected to decrease with increasing load. In other words, while the stitches significantly retard debond growth when they are carrying low loads, they have a decreased effect on strain energy release rate once they, and the debond front, are heavily loaded.

#### Effect of Increasing Debond Length

The third variable studied was the debond length. In this section, the debond length was allowed to increase with a fixed load of 500 lb./in. applied to the DCB. For the purposes of this discussion, a configuration corresponding to an intermediate DCB stiffness ( $t=0.220$  in.) was chosen. As shown in Figure 7(a), an unstitched DCB exhibits an increasing  $G_I$  with increasing debond length,  $a$ . In contrast, the slope of the  $G_I$  curve for the stitched DCB begins to decrease immediately after the debond front passes the location of the first stitch (first vertical line in Figure 7a) and the  $G_I$  curve may actually begin to decrease for debond lengths longer than approximately 0.25 in. (i.e.  $a/t=1.15$ ). The decrease in slope of the  $G_I$  curve is larger with both the number of loaded stitches and the distance from the debond front to each of the load-bearing stitches. Further, for long debonds ( $a/t>2.5$ ), the strain energy release rate is nearly zero.

The decrease in  $G_I$  for long debond lengths is the result of the stitches resisting debond opening (reducing the opening force in the region near the debond front.) This effect increases with increasing distance between the debond front and the stitch, and also with an increase in the number of load bearing stitches. Figure 7(b) shows how each of the stitches begins to carry load

as the debond of length,  $a$ , passes its location in the model. For example, the force in the first stitch ( $F_{axial}$ , *Stitch 1* in Figure 7b) starts at 0.0625 in. ( $a/t=0.284$ ) (point B) beyond the *Stitch 1* location (point A). Since the results were evaluated from the finite element model with increments of debond growth of 0.0625 in. ( $a/t=0.284$ ), the force in the stitch for debond lengths between points A and B is not known and is represented by the dashed line. The forces corresponding to the first 0.0625 in. ( $a/t=0.284$ ) of debond growth beyond the location of each successive stitch are represented in a similar manner. As seen in the figure, for short debond lengths, only the first row of stitches is loaded. As the debond length increases, the load is shared by additional rows of stitches.

### Mixed Mode Debond Models

The skin-stiffener configuration shown in Figure 2(b) exhibits both mode I and mode II deformations at the debond front. The configuration has a skin and a stiffener flange of equal thickness,  $t$ , of 0.220 inches. This mixed mode configuration is included to study the effect of increasing debond length on mixed-mode strain energy release rate and load carried in the stitches for a fixed applied load of 200 lb./in. As shown in Figure 8(a), both the mode I and mode II strain energy release rates,  $G_I$  and  $G_{II}$ , respectively, for the unstitched configurations increase with increasing debond length over the range of debond lengths,  $a$ , considered. The effect of the stitching on  $G_I$  in the mixed-mode configuration is very similar to that shown for the DCB in Figure 7(a).  $G_I$  initially increases with debond length and then begins to decrease after the debond passes the first stitch (first vertical line in Figure 8a), decreasing as additional stitches begin to carry load, eventually reaching near-zero values for long debonds ( $a/t > 2$ ). In contrast,  $G_{II}$  increases slightly with increasing debond length over the range of debond lengths considered. Thus, even though  $G_I$  is significantly reduced, there may be sufficient  $G_{II}$  present to grow the debond.

As seen in Figure 8(b), the axial force in the stitches ( $F_{axial}$ ) in the mixed mode configuration shows a similar behavior with increasing debond length as in the DCB configuration. In this configuration, however, a shearing force ( $F_{shear}$ ) is also present in the stitches, though it is smaller in both absolute and normalized magnitude than the axial force. As in the previous section, results were evaluated from the finite element model with increments of debond growth of 0.0625 in. ( $a/t=0.284$ ), so the force corresponding to the first 0.0625 in. ( $a/t=0.284$ ) of debond growth beyond a given stitch location in the finite element model was not recovered in the analysis

and is represented by the dashed lines in the figure. There are two ways that the debond may continue to grow in this mixed-mode configuration. If the stitches remain intact, the debond may continue to grow by mode II as shown in Figure 8(a). However, if the stitches fail, non-zero mode I may be present and may also contribute to the growth of the debond.

### Concluding Remarks

The effect of stitches on the mode I and mode II strain energy release rates of double cantilever beam and mixed-mode skin-stiffener debond configurations with an initial debond was studied. The plate element modeling technique was used to model the configuration and the virtual crack closure technique (VCCT) was used to calculate the strain energy release rates. Using this fracture mechanics approach, a debond between the skin and stiffener flange was assumed. The debond growth between the flange and the skin was assumed to be self-similar and continuous along the length of the flange-skin interface. The stitches were modeled as discrete nonlinear fastener elements with their compliance determined by experiment. Both axial and shear behavior of the stitches was considered, however, the two compliances and failure loads were assumed to be independent.

Stitches with stiffnesses in excess of 1,000 lb./in. in the 8 x 8 stitching pattern were required to noticeably affect the values of mode I strain energy release rate,  $G_I$ , for the double cantilever beam configurations studied. The effect of stitching was most significant for compliant DCB configurations. For fixed debond lengths, an increase in applied load results in an increase in the load carried by the stitches, thus, stitch compliance increases and contributes to an increase in  $G_I$ . However, if the debond length increases, additional stitches begin to carry load resulting in a decrease in  $G_I$ . For long debonds, the stitches may produce enough compressive force at the debond front to close the debond and reduce  $G_I$  to zero. Thus, failure of the stitches may be required to propagate the debond.

The mode I strain energy release rate computed for the mixed-mode debond configuration shows similar dependence on debond length as in the DCB. The stitches begin to carry considerable load and cause  $G_I$  to decrease once the debond length becomes sufficiently long. In contrast, the stitches have less effect on mode II and  $G_{II}$  increases throughout the range of debond lengths considered. Thus, there are two ways that the debond may continue to grow in this mixed-mode configuration. If the stitches do not fail, the debond

may continue to grow by mode II. However, if the stitches fail, non-zero mode I may be present and may also contribute to the growth of the debond.

### Acknowledgments

The authors wish to thank Drs. C.C. Rankin and R.D. Young for their many helpful discussions regarding the STAGS finite element code.

### References

1. Dow, M.B. and Dexter, H.B., "Development of Stitched, Braided and Woven Composite Structures in the ACT Program and at Langley Research Center," NASA TP-97-206234, November 1997.
2. Wang, J.T., Jegley, D.C., Bush, H.G. and Hinrichs, S.C., "Correlation of Structural Analysis and Test Results for the McDonnell Douglas Stitched/RFI All-Composite Wing Stub Box," NASA TM-110267, 1996.
3. Wang, J.T.S. and Biggers, S.B., "Skin/Stiffener Interface Stresses in Composite Stiffened Panels," *NASA CR 172261*, 1984.
4. Hyer, M.W. and Cohen, D., "Calculation of Stresses and Forces Between the Skin and Stiffener in Composite Panels," *28th AIAA/ASME/ASCE/AHS Structures, Structural Dynamics and Materials Conference*, AIAA Paper 87-0731-CP, 1987.
5. Cohen, D. and Hyer, M.W., "Influence of Geometric Nonlinearities on Skin-Stiffener Interface Stresses," *29th AIAA/ASME/ASCE/AHS Structures, Structural Dynamics and Materials Conference*, AIAA Paper 88-2217-CP, 1988.
6. Minguet, P.J., "Analysis of the Strength of the Interface between Frame and Skin in a Bonded Composite Fuselage Panel," *38th AIAA/ASME/ASCE/AHS Structures, Structural Dynamics and Materials Conference*, AIAA Paper 97-1342-CP, 1997, pp. 2783-2790.
7. Minguet, P.J. and O'Brien, T.K., "Analysis of Composite Skin-Stringer Bond Failures Using a Strain Energy Release Rate Approach," *Proceedings of the Tenth International Conference on Composite Materials*, Vol. I, Woodhead Publishing Ltd., 1995, pp. 245-252.
8. Minguet, P.J. and O'Brien, T.K., "Analysis of Test Methods for Characterizing Skin/Stringer Debonding Failures in Reinforced Composite Panels," *Composite Materials: Testing and Design*, Twelfth Volume, ASTM STP 1274, August 1996, pp. 105-124.
9. O'Brien, T.K., "Characterization of Delamination Onset and Growth in a Composite Laminate," *Damage in Composite Materials, ASTM STP 775*, 1982, pp. 140-167.
10. Wang, A.S.D. and Crossman, F.W., "Initiation and Growth of Transverse Cracks and Edge Delamination in Composite Laminates, Part 1: An Energy Method," *Journal of Composite Materials*, Vol. 14, 1980, pp. 71-87.
11. Whitcomb, J.D., "Instability-Related Delamination Growth of Embedded and Edge Delaminations," *NASA TM 100655*, 1988.
12. Wang, J.T., Raju, I.S., and Sleight, D.W., "Composite Skin Stiffener Debond Analyses Using Fracture Mechanics Approach with Shell Elements," *Composites Engineering*, Vol. 5, No. 2, 1995, pp. 277-296.
13. Raju, I.S., Sistla, R., Krishnamurthy, T., "Fracture Mechanics Analyses for Skin-Stiffener Debonding," *Engineering Fracture Mechanics*, Vol. 54, No. 3, 1996, pp. 371-385.
14. Wang, J.T., Raju, I.S., Davila, C.G. and Sleight, D.W., "Computation of Strain Energy Release Rates for Skin-Stiffener Debonds Modeled with Plate Elements," *34th AIAA/ASME/ASCE/AHS Structures, Structural Dynamics and Materials Conference*, AIAA Paper 93-1501-CP, 1993, pp. 1680-1692.
15. Wang, J.T. and Raju, I.S., "Strain Energy Release Rate Formulae for Skin-Stiffener Debond Modeled with Plate Elements," *Engineering Fracture Mechanics*, Vol. 54, No. 2, 1996, pp. 211-228.
16. Glaessgen, E.H., Riddell, W.T. and Raju, I.S., "Effect of Shear Deformation and Continuity on Delamination Strain Energy Release Rate," *39th AIAA/ASME/ASCE/AHS Structures, Structural Dynamics and Materials Conference*, AIAA Paper 98-2023-CP, 1998.
17. Mignery, L.A., Tan, T.M., and Sun, C.T., "The Use of Stitching to Suppress Delamination in Laminated Composites," *ASTM STP 876*, 1985, pp. 371-385.
18. Chen, V.L., Wu, X.X., and Sun, C.T., "Effective Fracture Toughness in Stitched Laminates," *Proceedings of the Eighth Technical Conference of the ASC*, 1994, pp. 453-462.
19. Sharma, S.K. and Sankar, B.V., "Effects of Through-the-Thickness Stitching on Impact and

Interlaminar Fracture Properties of Textile Graphite/Epoxy Laminates," *NASA CR195042*, 1995.

20. Sankar, B.V. and Sonik, V., "Modeling End-Notched Flexure Tests of Stitched Laminates," *Proceedings of the American Society for Composites*, ASC, 1995, pp. 172-181.

21. Byun, J.-H., Gillespie, Jr., J.W. and Chou, T.-W., "Mode I Delamination of a Three-Dimensional Fabric Composite," *Journal of Composite Materials*, Vol. 24, May 1990, pp. 497-518.

22. Tsai, G.C., "Global/Local Stress Analysis of Stitched Composite Laminates," *Proceedings of the 23rd International SAMPE Technical Conference*, SAMPE, 1991, pp. 297-305.

23. Lee, C. and Liu, D., "Tensile Strength of Stitching Joint in Woven Glass Fabrics," *Journal of Engineering Materials and Technology*, Vol. 112, April 1990, pp. 125-130.

24. Rybicki, E.F. and Kanninen, M.F., "A Finite Element Calculation of Stress Intensity Factors by a Modified Crack Closure Integral," *Engineering Fracture Mechanics*, Vol. 9, 1977, pp. 931-938.

25. Raju, I.S., "Calculation of Strain-Energy Release Rates with Higher Order and Singular Finite Elements," *Engineering Fracture Mechanics*, Vol. 28, No. 3, 1987, pp. 251-274.

26. Brogan, F.A., Rankin, C.C., Cabiness, H.D. and Loden, W.A., *STAGS User Manual*, Lockheed Martin Missiles and Space Co., July 1996.

27. Young, R.D., Rankin, C.C., Starnes, J. and Britt, V., *Introduction to STAGS*, Lecture Notes from a Workshop at NASA Langley Research Center, Hampton, VA, March 8-9, 1995.

28. Davis, J.G., Shuart, M.J. and Bowles, D.E., Eds., *Fifth NASA/DoD Advanced Composites Technology Conference*, NASA CP 3294, May 1995.

29. Adams, D.O., "Stitch Compliance in Delaminated Composites," *29th SAMPE Technical Conference*, Orlando, FL, October 28-31, 1997.

30. Reinhart, T.J., *Engineered Materials Handbook, Vol. 1 Composites*, ASM International, 1987.

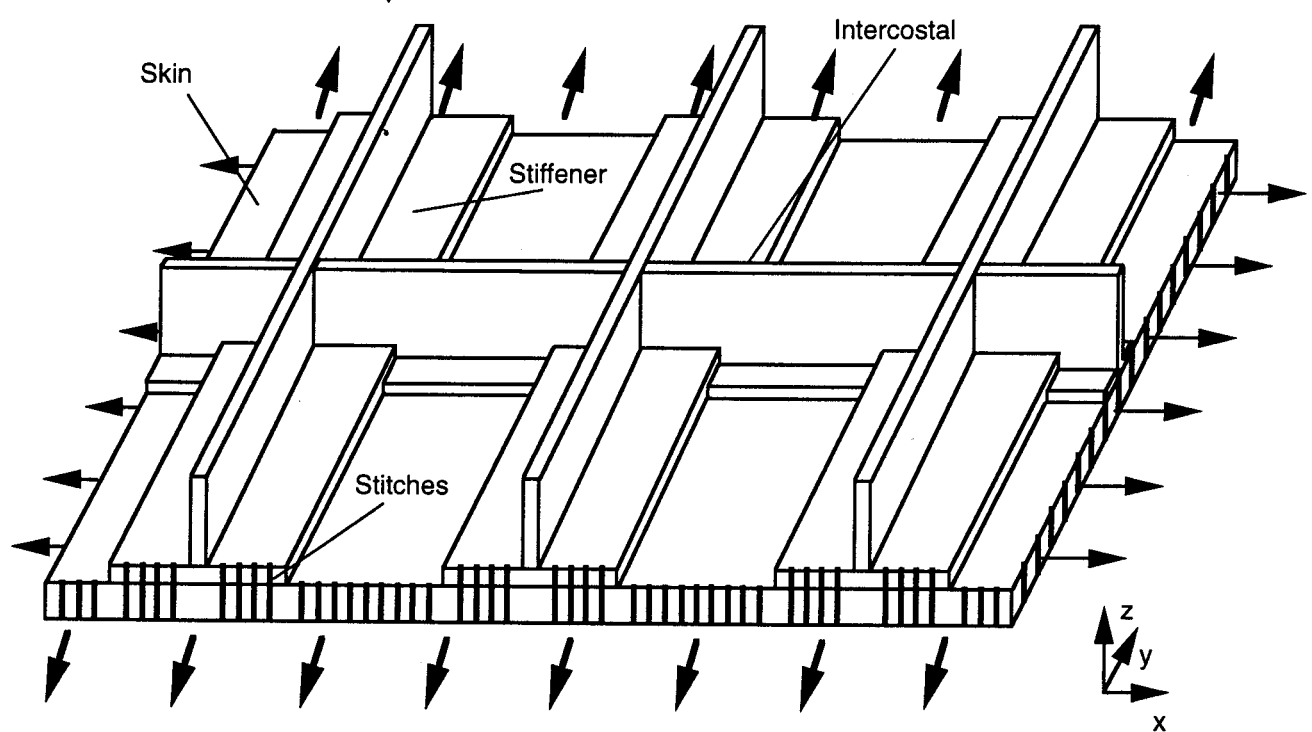


**Figure 1 Stitched composite panel with stiffeners**



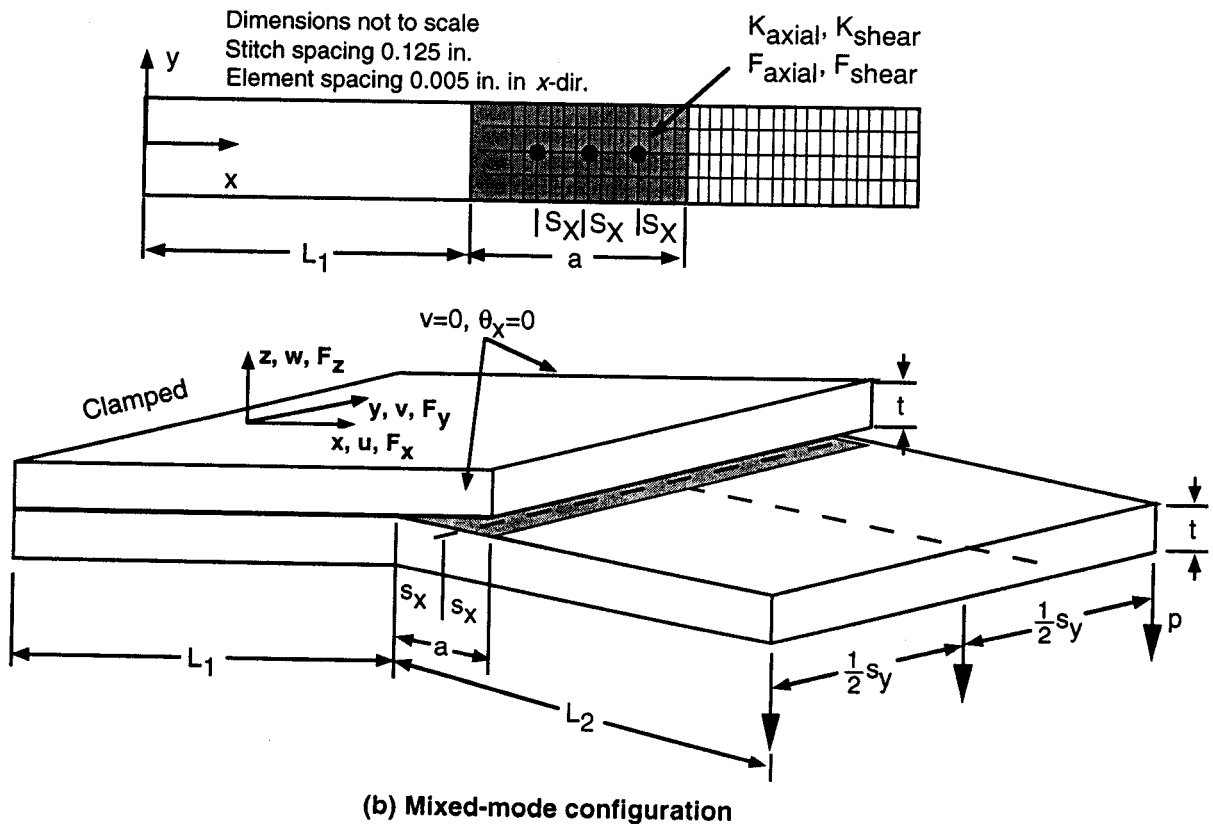
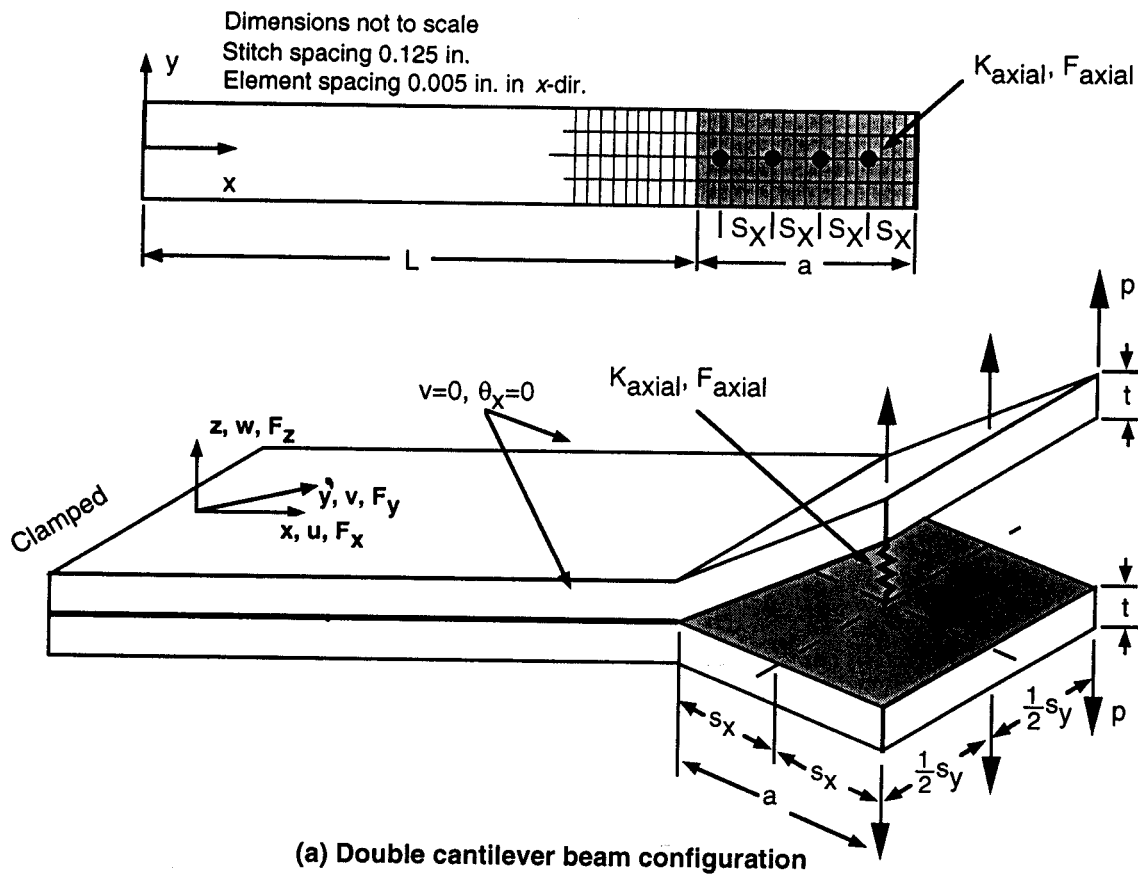
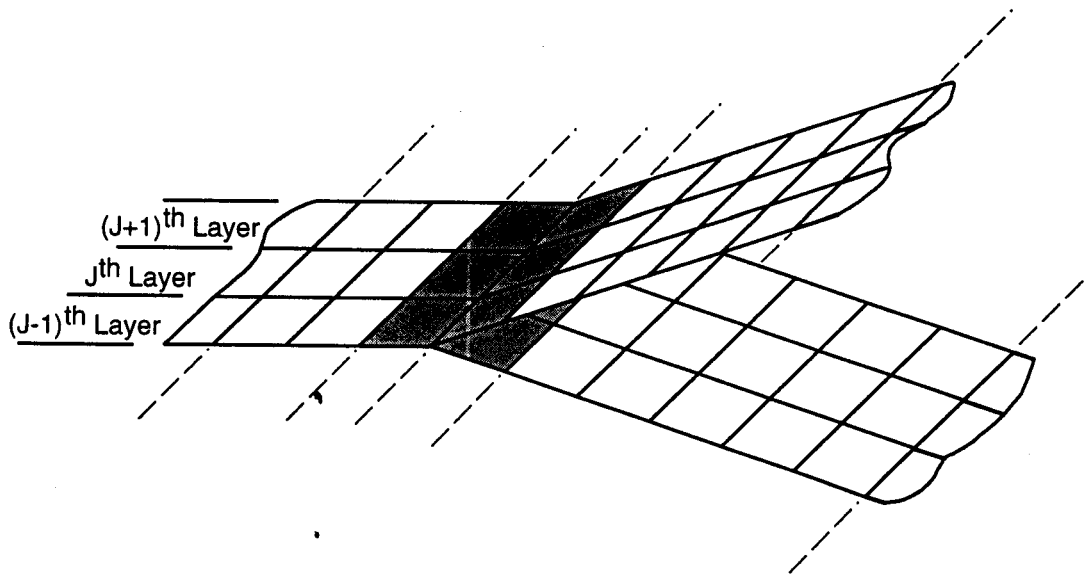
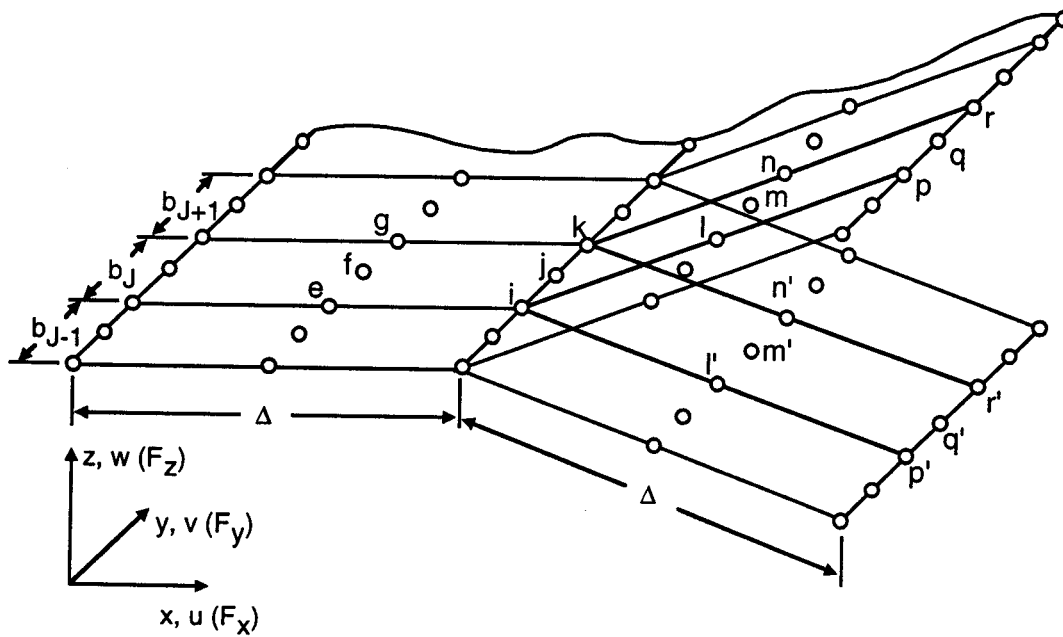


**Figure 2 Debond configurations**

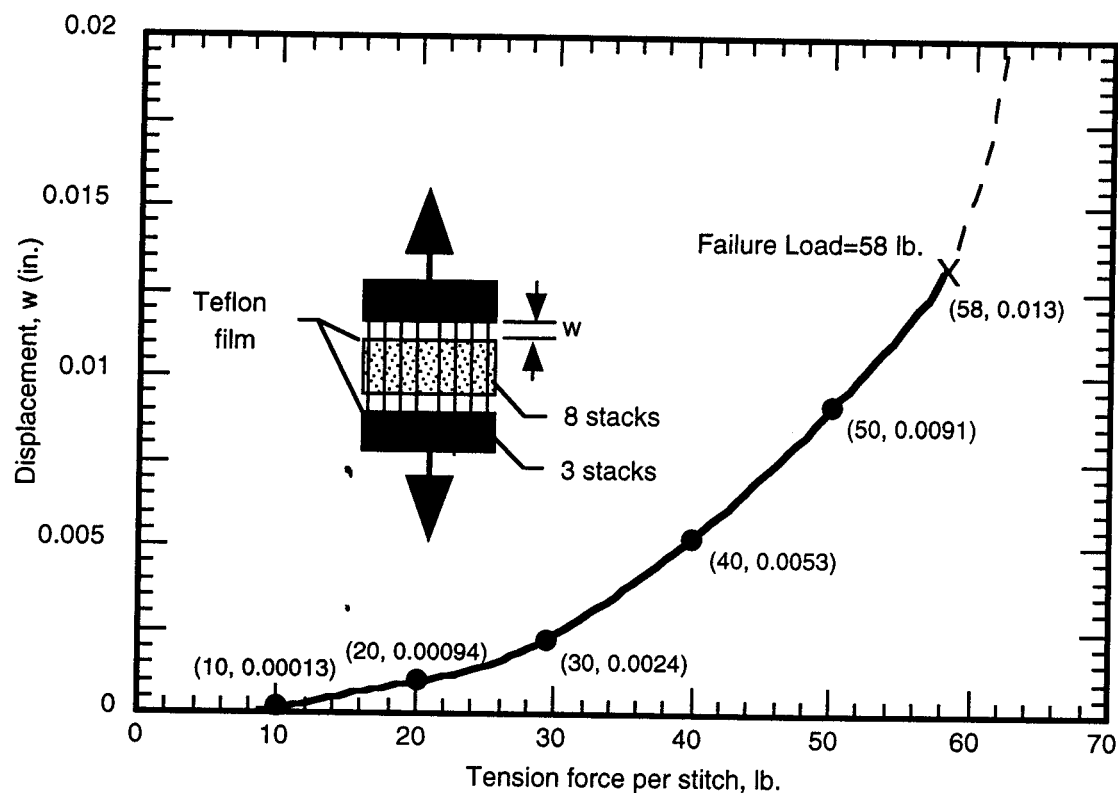


(a) Plate element modeling near the debond front

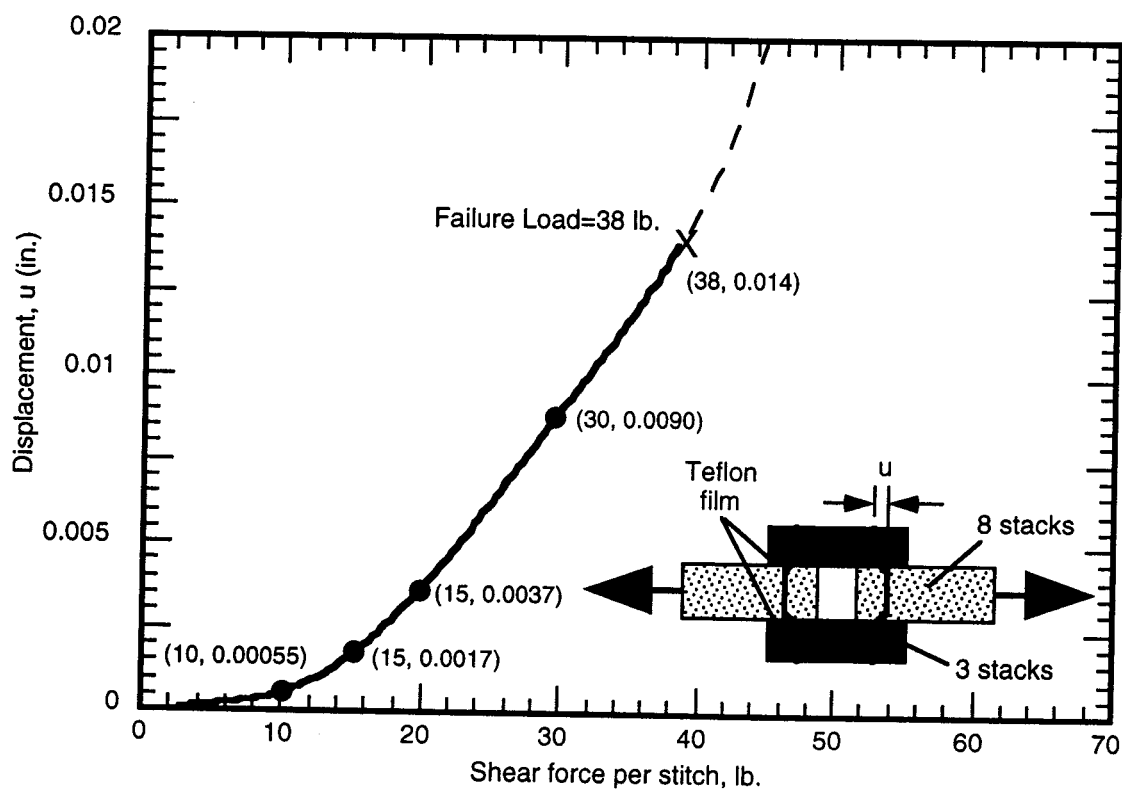


(b) Details of the model near the debond front

Figure 3 Debond configuration modeled using 9-node plate elements

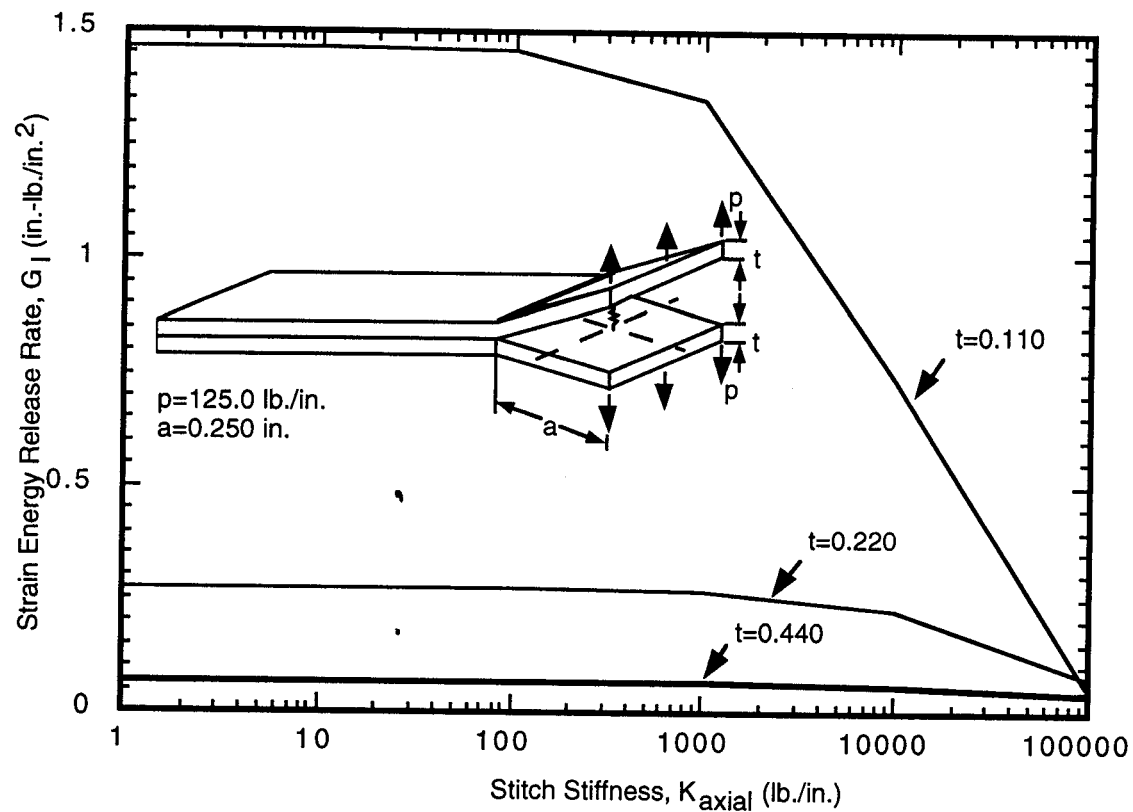


(a) Compliance of stitches in tension

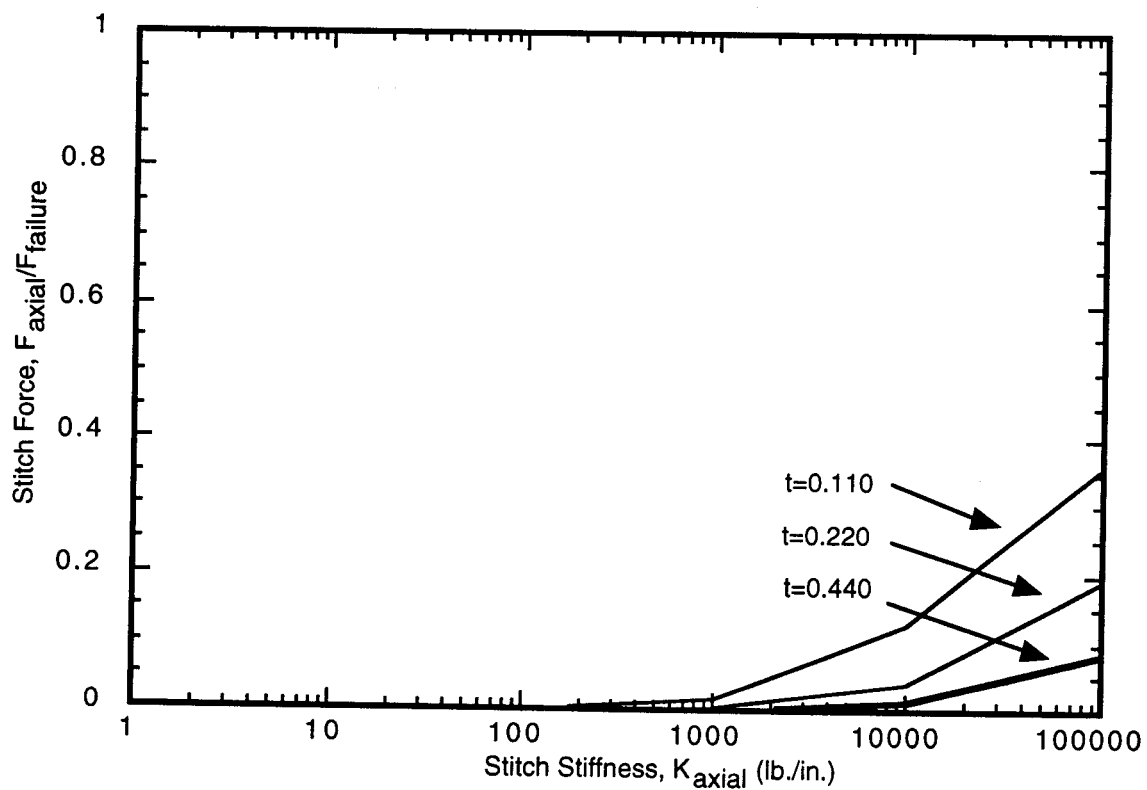


(b) Compliance of stitches in shear

Figure 4 Stitch compliance (experimental results taken from reference 25)

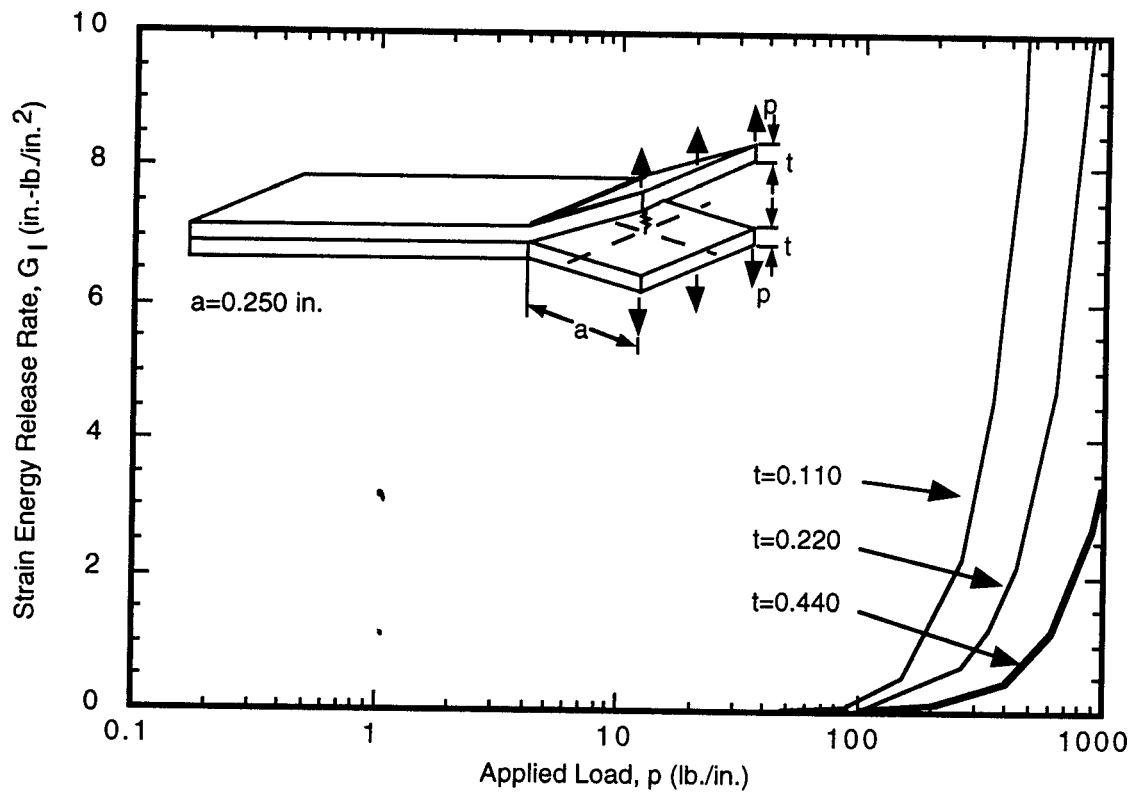


(a) Strain energy release rate for a range of stitch stiffnesses

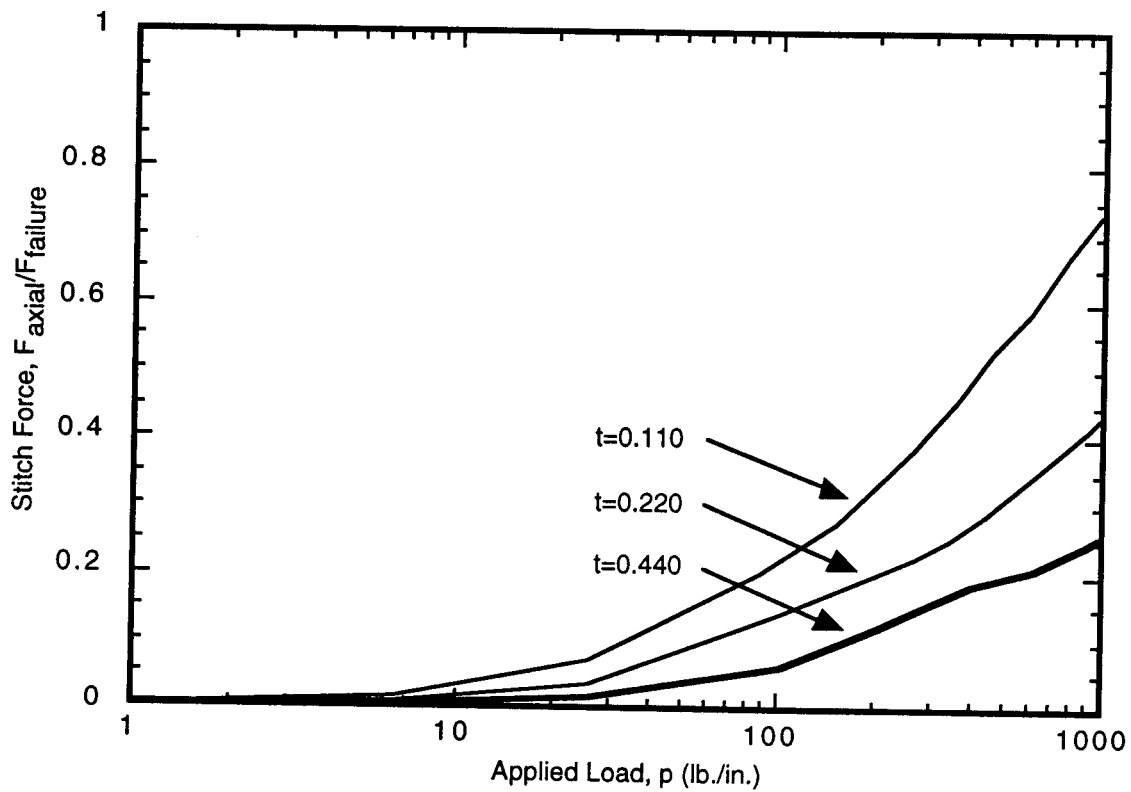


(b) Stitch force for a range of stitch stiffnesses

Figure 5 Effect of stitch stiffness on strain energy release rate and stitch force  
(Applied Load,  $p=125.0$  lb./in.,  $a=0.250$  in.,  $s_x=0.125$  in.,  $s_y=0.125$  in.)

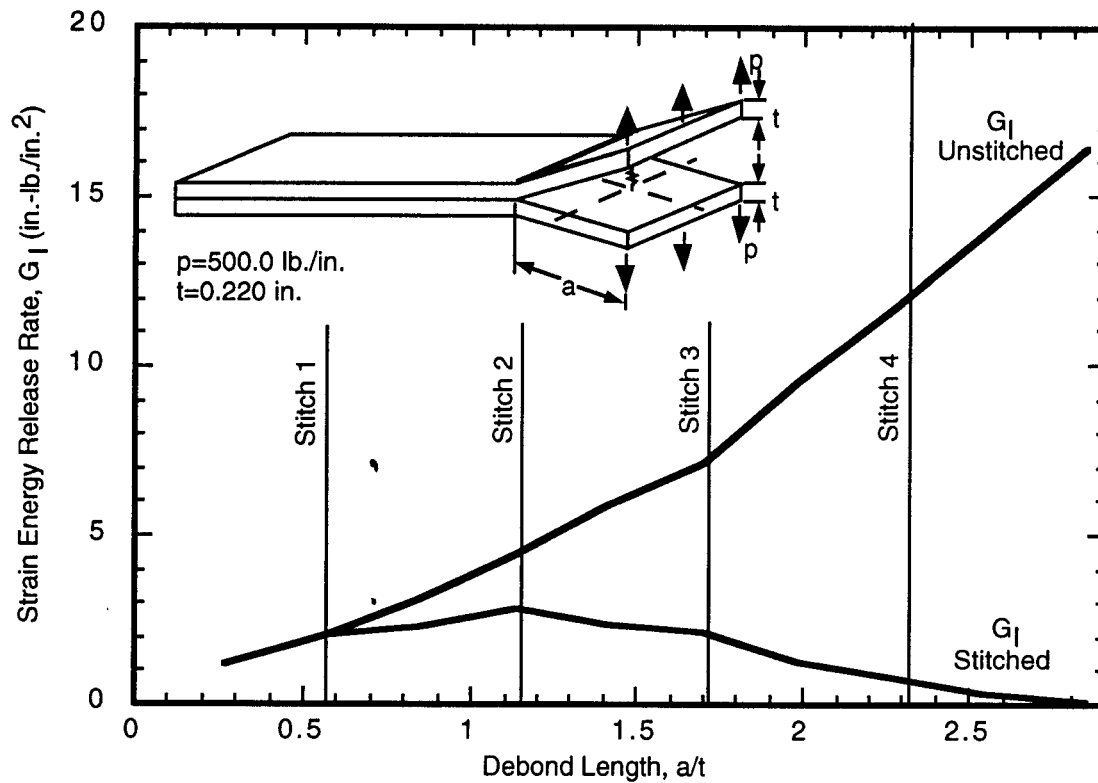


(a) Strain energy release rate as a function of applied load

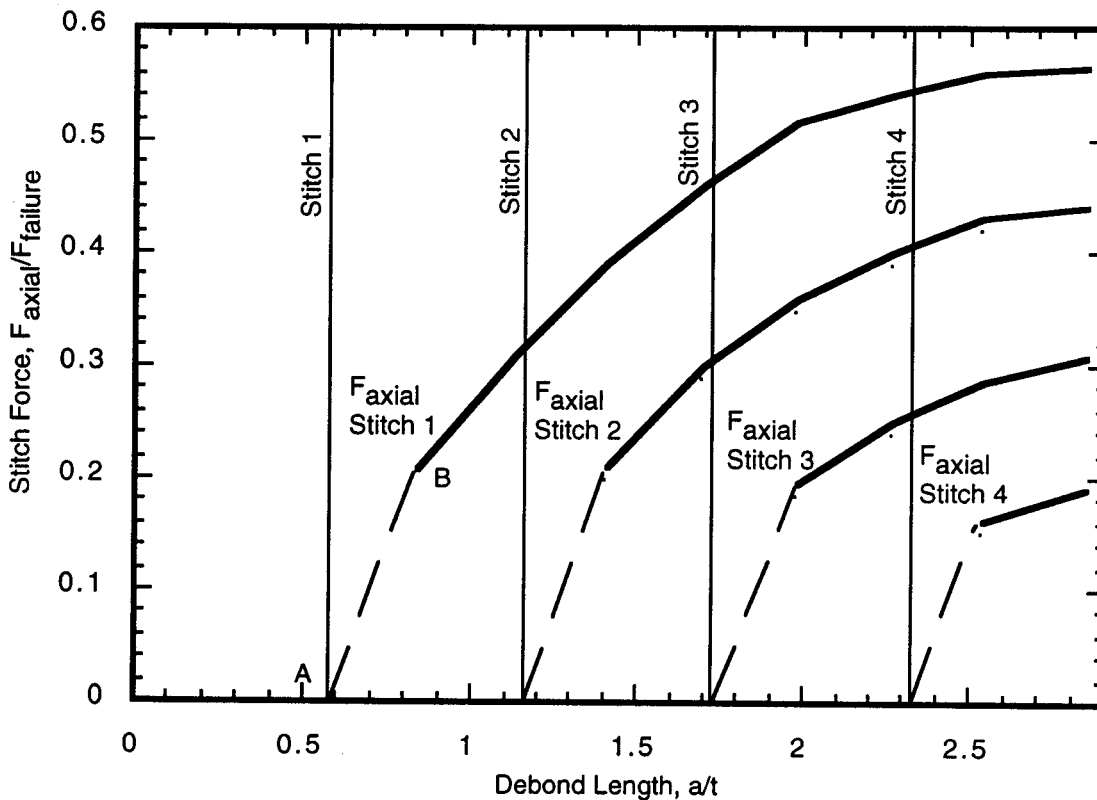


(b) Stitch force as a function of applied load

Figure 6 Effect of applied load on strain energy release rate and stitch force  
 ( $a=0.250$  in.,  $s_x=0.125$  in.,  $s_y=0.125$  in.)

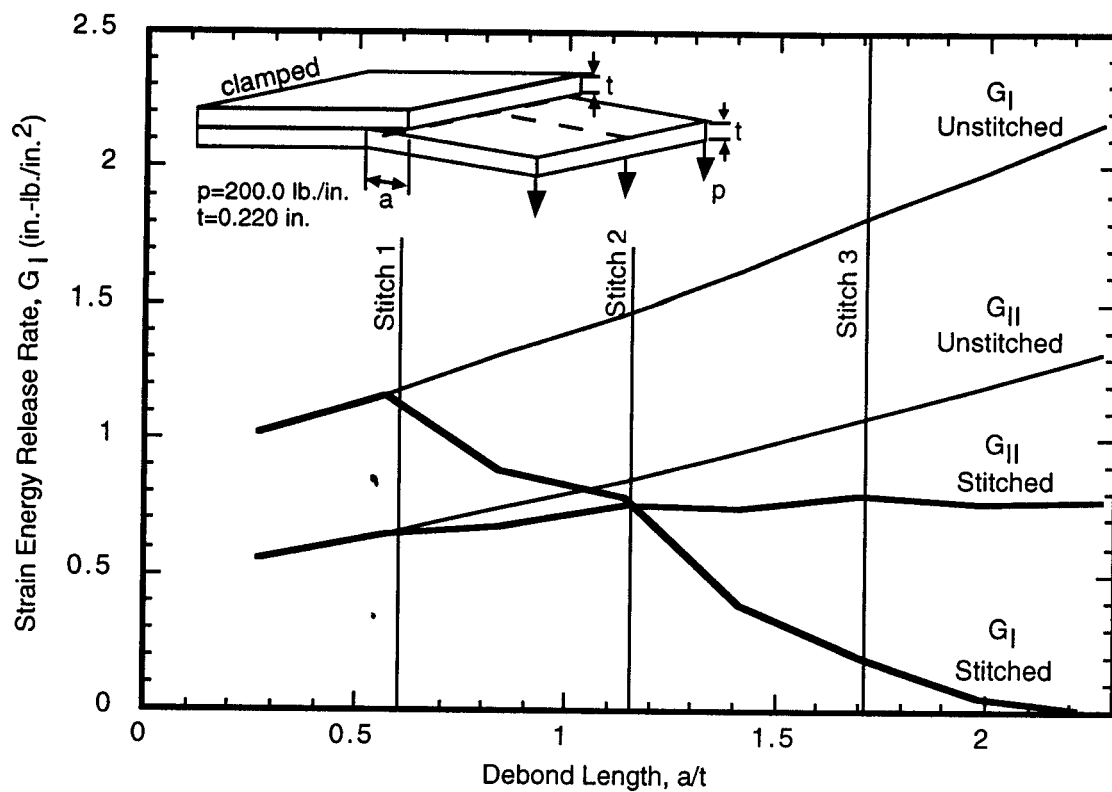


(a) Strain energy release rate as a function of debond length

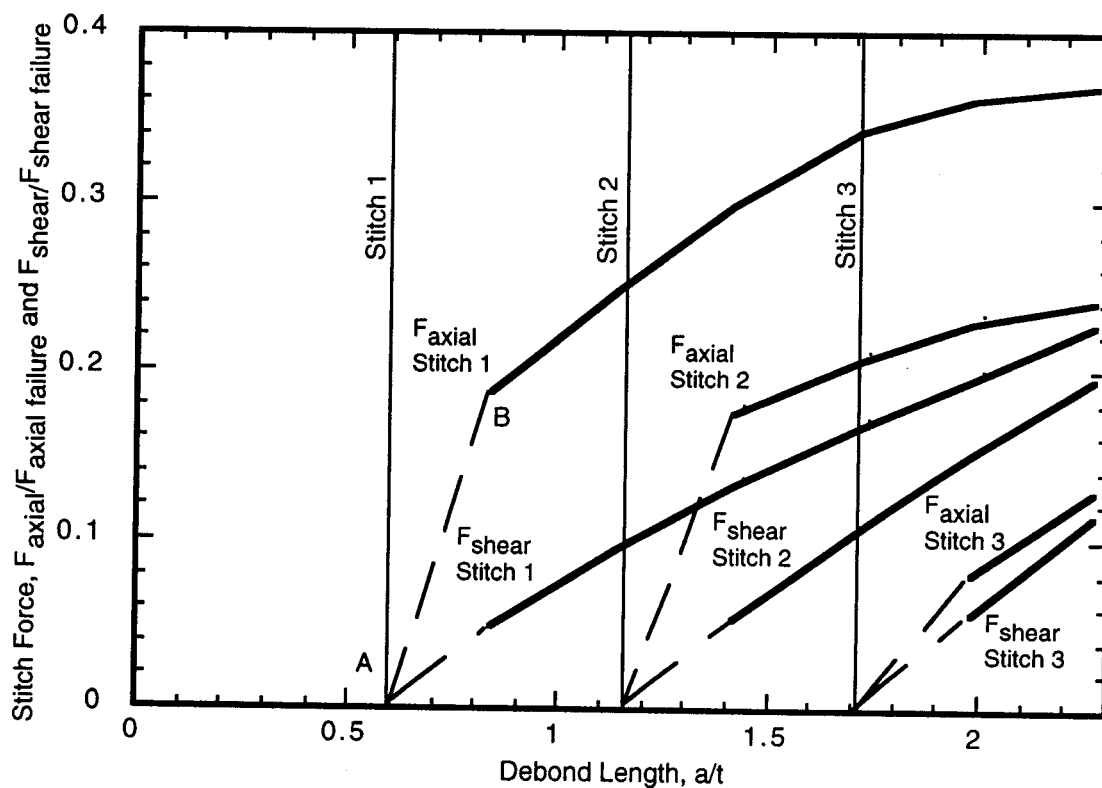


(b) Stitch force as a function of debond length

Figure 7 Effect of debond length on strain energy release rate and stitch force  
(Applied Load,  $p=500.0$  lb./in.,  $t=0.220$  in.,  $s_x=0.125$  in.,  $s_y=0.125$  in.)



(a) Strain energy release rate as a function of debond length



(b) Stitch force as a function of debond length

Figure 8 Effect of multiple stitches on  $G_I$ ,  $G_{II}$  and stitch force  
(Applied Load,  $p=200.0$  lb./in.,  $t=0.220$  in.,  $s_x=0.125$  in.,  $s_y=0.125$  in.)